Microporous and Mesoporous Materials 158 (2012) 195–203

Contents lists available at SciVerse ScienceDirect

Microporous and Mesoporous Materials

journal homepage: www.elsevier.com/locate/micromeso

Molecular modeling of carbon dioxide transport and storage in porous carbon-based materials

Mahnaz Firouzi, Jennifer Wilcox *

Department of Energy Resources Engineering, Stanford University, Stanford, CA 94305-2220, USA

ARTICLE INFO

Article history:
Received 2 May 2011
Received in revised form 27 December 2011
Accepted 29 February 2012
Available online 7 March 2012

Keywords:
ECBM
CO_2 sequestration
NEMD
Molecular dynamics
CO_2 permeability

ABSTRACT

To fundamentally study the molecular processes in porous carbon-based systems relevant to transport and storage of carbon dioxide, non-equilibrium molecular dynamics simulations have been carried out with an external driving force imposed on a carbon-based 3-D pore network. The purpose of this study is to investigate the transport properties of pure carbon dioxide, methane and nitrogen as well as binary mixtures nitrogen and carbon dioxide and also methane and carbon dioxide through modeled 3-D carbon-based systems representative of porous carbon-based materials. The 3-D pore network has been generated atomistically using the Voronoi tessellation method of a structure containing approximately 125,000 atoms. Simulations have been carried out to determine the effect of the pore structure, exposure to an external potential and composition mixture on phenomena such as fluid distribution in the system and permeability for broad ranges of conditions. The results indicate that the morphological characteristics and energetic effects play a dominant role in the flow and transport properties of fluids. As expected among these factors, the porosity of the structure strongly affect the permeability. In addition, our simulation results indicate that the permeability is *zero* below a critical porosity of about 0.2 due to the low connectivity in the pore network.

1. Introduction

Transport and separation of carbon dioxide (CO_2) in microporous carbon-based materials is an industrially important problem, particularly for the mitigation of greenhouse emissions, which is currently of fundamental and practical interest [1]. Carbon storage has the capacity to potentially mitigate gigatons of CO_2 emissions (estimates of the potential geological storage capacity range from 1700 to 11,100 $GtCO_2$ equivalent, or from 70 to 450 years of 2003-level fossil-fuel-related emissions, which is equivalent to 24.5 $GtCO_2$/year) [2,3]. However, technical obstacles have thus far hindered wide-scale deployment of this strategy. It is important to understand the chemical and physical properties of CO_2 and its interaction with its local surroundings on the molecular-scale to design efficient and reliable strategies for carbon storage at full-scale. Gas storage could occur through surface adsorption, absorption, and confinement depending on the pore structure of storage media and pore surface chemistry. Surface adsorption provides the basis for storage in microporous materials with large surface area where the adsorbent–adsorbate interaction is of crucial importance. For porous materials with smaller surface area, surface adsorption becomes less effective for gas storage. Surface functional groups present within the pores of a porous material may serve as active sites for adsorption [4,5]. In particular, CO_2 storage in deep unminable coalbeds has been proposed as an alternative option to reduce anthropogenic CO_2 emissions. Substantial amounts of gas, mostly methane, are known to be adsorbed or dispersed within the pore spaces of deep (300 to 1500 m) coal seams. Enhanced coalbed methane (ECBM) projects aim to displace methane by CO_2. It has been shown that almost 2–10 times as much of methane gas can be stored in coalbeds using ECBM [6–11]. The sorption and diffusion behaviors of CO_2 and CH_4 on coal were investigated at the molecular level using molecular dynamics indicating that the diffusion of CH_4 is slightly faster than that of CO_2 and that the calculated sorption heat of CO_2 was larger than that of CH_4, which could be the reason why CO_2 can displace adsorbed CH_4 gas in coal, thus enhancing the recovery of CH_4 [12]. To date, low permeabilities of coal have been a major issue in preventing commercial gas production. Fundamental understanding of the microstructures of coal and its influence on transmissibility of methane is of great importance in the recovery of this valuable resource [13]. To understand the molecular processes relevant to storage of CO_2 in unminable coal seams with enhanced methane recovery, gas transport phenomena in the coal matrix requires further investigation.

Coals are porous materials with porosity and pore size distributions varying throughout. For instance, pores in coal vary in size from micrometers to angstroms in dimension. A significant proportion of their total open pore volume is located in small pores of less

* Corresponding author. Tel.: +1 650 724 9449
E-mail address: jen.wilcox@stanford.edu (J. Wilcox).

1387-1811/$ - see front matter © 2012 Elsevier Inc. All rights reserved.
http://dx.doi.org/10.1016/j.micromeso.2012.02.045

than 20 Å in diameter [14,15]. Pore size is classified into four groups: macropores which are larger than 500 Å, mesopores which are between 20 and 500 Å, micropores which are between 8 and 20 Å, and submicropores which are less than 8 Å [16]. Quantifying pore size distribution, pore connectivity and porosity is desirable to determine the difference between how gases such as methane and CO_2 sorb and permeate in these systems [11].

Coal's porosity is a strong and nonlinear function of its rank measured by carbon content and lithotype/maceral and mineral composition. The porosity may vary from 4% to 20% [15,17,18]. For high-rank coals, the total porosity could be 4–8% [15]. For low to medium-rank coals, such as lignite and bituminous, the total porosity could be between 15% and 20% [17,19]. Cleat-fracture porosity in coal is estimated to be between 0.5% and as much as 2.5% [20–23]. In other studies conducted by Advanced Resources International [24] and Mavor et al. [25] it was determined through history-matching of gas and water production from wells in the Powder River Basin (PRB), the porosity in the cleats is reported to range from 0.1 to 6%, whereas coal matrix porosities range from 1–10%.

For the creation of realistic carbon models for CO_2 separation and storage applications, determining the pore size distribution and connectivity is challenging. Several recent studies [26,27] have investigated the molecular sorption process in coal through molecular modeling approaches, and reported complex phenomena addressing morphology changes associated with sequestration. They investigated the sorptive capacity of a bituminous coal model for both CO_2 and CH_4, swelling of the structure caused by CO_2, micropore accessibility, and the role of moisture in sequestration [26]. Also, adsorption has been investigated on a molecular scale to identify energetically favorable adsorption sites [27]. In another study, the hybrid reverse Monte Carlo method has been adapted to develop a detailed atomistic model of Calgon Company's bituminous coal-based activated carbon (BPL) microstructure to predict adsorptive behavior using grand-canonical Monte Carlo (GCMC) simulations [28]. With these previous studies focusing primarily on sorption behavior, there is currently little fundamental knowledge on fluid transport in these carbon-based porous systems at the molecular scale due to their complex morphology and chemical make-up. The current work represents the next steps in understanding the phenomena involved during the transport of fluid mixtures in carbon-based 3-D pore network models.

These studies offer unique insight into the behavior of gases inside porous carbon-based materials such as sorbents and simplified structures representative of high-rank coals. The purpose of this study is to create a set of realistic models in an attempt to shed light on the details of transport and storage processes at the atomistic level.

Molecular modeling studies are based on non-equilibrium molecular dynamics (NEMD) simulations, a technique ideally suited for the experimental scenario in which an external driving force, such as a chemical potential or pressure gradient, is applied to the porous structure. A dual control volume grand-canonical MD (DCV-GCMD) technique, which has been used extensively [29–51] has been utilized. Although applications of the current work span carbon capture and storage applications, focus will be on temperature and pressure conditions directly applicable to CO_2 storage in unminable coalbeds.

2. Molecular pore network model

Transport and adsorption properties of CO_2, methane and nitrogen in activated carbon, and the organic matrices of coal and gas shale rocks are strongly influenced, and sometimes even dominated, by the morphology of their structure, which consist of the connectivity of its pores, and their shapes, sizes and surface characteristics. The structure of real disordered porous solids is very complicated and may not be represented by a single pore. The main source of heterogeneity in these systems is their complex porous structure, which contains pores of different sizes and shapes, including straight and tortuous pathways, and contracting and diverging channels. When such single pores are connected, they form pore networks. The realistic simulation of porous materials addresses two important aspects, i.e., the modeling of the solid material itself and the generation of its pore structure including pore size distribution and pore-network connectivity. The most direct route towards addressing both of these aspects is through the atomistic simulation of these materials. To address the problem of correct representation of the morphology of these complicated structures, in this paper we describe an efficient molecular pore-network model for porous materials, and in particular of carbon-based materials with a pore space that contains pores of irregular shapes and sizes that follow a certain pore size distribution (PSD). The pore networks are generated by the Voronoi tessellation of a solid material composed of hundreds of thousands of atoms, and by designating a fraction of the Voronoi polyhedra as the pores. The model allows for the investigation of the effect of the morphology of the pore space, i.e., its pore size distribution and pore connectivity, on the adsorption and transport of methane and CO_2 for capture and storage applications. The molecular pore network is generated based on geometric considerations alone and the chemical and energetic details of creating the nanopores are ignored. In this method, we begin with a 3-D cell of carbon atoms with a structure corresponding to graphite so that the number density of carbon atoms is 114 nm^{-3} and the spacing between the adjacent graphite layers in the z direction is 0.335 nm. The size of the initial graphite cell is 102, 103, and 103 Å in x, y, and z directions, respectively, and consisting of 124,992 carbon atoms. Periodic boundary conditions were applied in all directions. The graphite cell is then tessellated through the insertion of a given number of Poisson points at random positions inside the simulation cell, each of which is used for constructing a 3-D Voronoi polyhedron, such that every point inside each polyhedron is closer to its own Poisson point than to any other Poisson point. The pore space is then generated by fixing its desired porosity and selecting a number of polyhedra, that can be chosen randomly or by first sorting and listing the polyhedra in the cell according to their sizes from smallest to largest (or vice versa), in such a way that their total volume fraction equals the desired porosity. The polyhedra, so chosen, are then designated as the pores by removing the carbon atoms comprising them, as well as those that are connected to only one neighboring carbon atom (the dangling atoms, i.e., connected to only one other atom). In fact, the removal of the dangling atoms was necessary since in a real porous material, it is physically impossible to have such atoms connected to the internal surface of the pores. Also, removal of the dangling atoms gives rise to pore surface roughness at the micro-level, which is expected to exist in any real pore [46,52,53].

The remaining carbon atoms constitute the solid matrix, while the pore space consists of interconnected pores of various shapes and sizes. The equivalent radius size of each polyhedron is taken to be the radius of a sphere that has the same volume as the polyhedron. If the pore polyhedra are selected at random, then, assuming that the size of the simulation cell is large enough, their size distribution will always be Gaussian, regardless of the porosity of the pore space. The 3-D graphite pore networks with desired porosities can be generated using this model. In addition, any desired average pore size can be fixed by varying the number of Poisson points inside the initial graphite cell. Clearly, the larger the number of Poisson points, the smaller the average pore size.

Fig. 1 represents the computed pore size distributions (PSDs) of different pore network models when the porosity is 15% and the pores are selected randomly, with average pore sizes of 12, 16, 20, and 24 Å, respectively. The number of inserted Poisson points in the simulation cell for the average pore sizes of 12, 16, 20, and 24 Å are 1000, 460, 240, 140, respectively. In order to plot the distribution, the pore size range was divided into 2-Å intervals.

The pore space generated by these models is a molecular-scale pore network, unlike the traditional pore networks that are used in the simulation of flow and transport in microporous media, this allows accounting for the interaction of the fluid molecules with all the atoms in the structure. We should point out that the Voronoi network has been previously utilized as a prototype of irregular networks to study transport in disordered composites [54–56]. In addition, the statistics of Voronoi tessellations have been used in the past to characterize the porosity distribution in porous materials [46,57–60]. In the previous studies [59,60] a binary fluid mixture in which one of the components serves as a template material was simulated. By removing the template particles from the mixture, the final porous material was then generated. However, the method that we propose in this paper is different from the previous studies [59,60]. Here, we first develop the atomistic model of the porous material by molecular simulation, and then generate the inherent porosity by tessellating the resulting porous molecular structure. The Voronoi structure has also been used in the past for modeling of polymer membrane and adsorption systems. The atomistic Voronoi structure has been developed to model carbon membranes to study the transport and adsorption of the gases, including the existence of an optimal pore structure for maximum separation of the gases [46]. The Voronoi model has also been utilized to compute the adsorption isotherms of N_2 in three distinct silicon–carbide (SiC) membranes at 77 K, and transport and separation of H_2/CO_2 and H_2/CH_4 mixtures and found good agreement with the experimental data [52,53].

The pore space of many natural porous materials, ranging from biological materials, wood, and foam [61,62], to sandstone and other types of rock [63], can be well represented by Voronoi-type structures. Additionally, the Voronoi algorithm has great flexibility in terms of constructing disordered pore networks with many variations in the sizes and shapes of the polyhedra. The algorithm can be modified to generate pore polyhedra with a great variety of shapes, from completely random to very regular shapes [64]. Previous studies include a comparison of the computed PSD for the model carbon molecular sieve membrane (CMSM) using the Voronoi tessellation to the experimentally measured PSD of a typical CMSM [47], which are in good agreement [65].

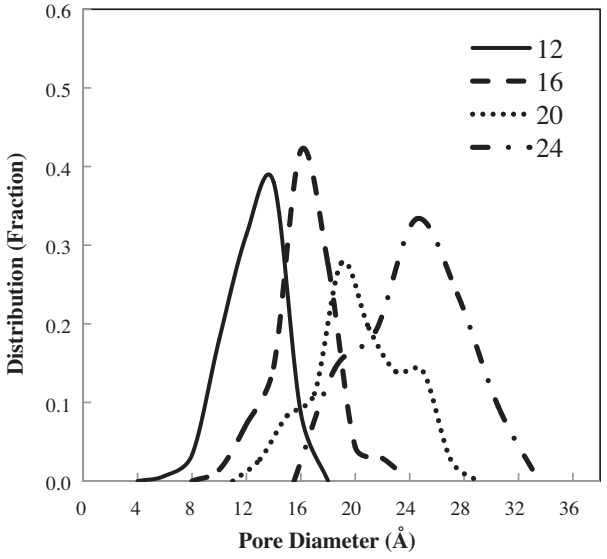

Fig. 1. Computed pore size distribution (PSD) of the pore network with the average pore sizes 12.5 Å (solid curve), 16.2 Å (dashed curve), 20.4 Å (dotted curve), and 24.3 Å (dashed-dotted curve). The porosity is 15%, and the pores are selected randomly.

3. The molecular modeling method

In the simulation we used the dual control volume grand-canonical molecular dynamics DCV-GCMD method, which combines the MD moves in the entire system with GCMC insertions and deletions of the molecules in the two control volumes (CVs). In this model the pore network structure is connected to two CVs that are exposed to the bulk fluid at high and low chemical potentials (μ) or pressures (P). The external driving force is a chemical potential or pressure gradient applied in the x direction. It is essential to maintain the densities (or the corresponding chemical potentials) of the components in the CVs at some fixed values, which are in equilibrium with two bulk phases, each at a fixed pressure and fluid concentration by carrying out a sufficient number of GCMC insertions and deletions of the particles. The probability of inserting a particle of component i is given by Eq. (1):

$$P_i^+ = \min\left\{\frac{Z_i V_c}{N_i + 1}\exp(-\Delta U/k_B T), 1\right\}, \quad (1)$$

where $Z_i = \exp(\mu_i/k_B T)/\Lambda_i^3$ is the absolute activity at temperature T, Λ_i and μ_i are, respectively, the de Broglie wavelength (Λ_i) and chemical potential of component i, k_B the Boltzmann's constant, ΔU the potential energy change resulting from creating or removing a particle, and V_c and N_i are the volume of the CV and number of atoms of component i in each CV, respectively. The probability of deleting a particle is given by Eq. (2):

$$p_i^- = \min\left\{\frac{N_i}{Z_i V_c}\exp(-\Delta U/k_B T), 1\right\}, \quad (2)$$

The chemical potentials were converted to equivalent pressures using a Lennard-Jones (LJ) equation of state [66]. When a particle is inserted in a CV, it is assigned a thermal velocity selected from the Maxwell–Boltzmann distribution at the given T. Typically, 10 GCMC insertions and deletions in each CV were followed by one MD integration step. In the MD simulations the Verlet velocity algorithm was used to integrate the equations of motion with a dimensionless time step, $\Delta t^* = 5 \times 10^{-3}$ (i.e., $\Delta t = 0.00685$ ps). The most demanding aspect of the simulations is the computation of nonbonded interactions, since millions of pairs have to be evaluated at each time step. Extending the time step is thus an important way to improve the simulation performance; however, the time step can be increased as much as possible without jeopardizing energy conservation. In the current and previous work [48,50], the time step in the Verlet algorithm is based on the modeling details to speed up the calculation and also to minimize the simulation error. The equations of motion were integrated with up to 10^7 time steps to ensure that steady state has been reached. Steady state was typically reached in the system after 5–6 million time steps; however, the simulation is continued up to 10^7 time steps, after which the properties, such as concentration profiles, fluxes, etc. were calculated and averaged over the last one million time steps. During the MD calculations molecules that crossed the outer boundaries of the CVs were removed. However, the number of such molecules was very small, typically about 1% of the total number of molecules that were deleted during the GCMC simulations. To study the transport of a fluid due to a pressure gradient, the temperature of the system was held constant to eliminate any

contribution of the temperature gradient to the transport; hence, iso-kinetic conditions were maintained by rescaling the velocity independently in all the three directions.

4. Molecular models of the gases and the interaction potentials

The molecules CO_2, CH_4, and N_2, as well as the carbon atoms comprising the pore surfaces, are represented using LJ potentials and characterized by the effective LJ size and energy parameters, σ and ε, respectively [67]. We used $\sigma_c = 3.4$ Å, and $\varepsilon_c/k_B = 28$ K for the carbon atoms constituting the pore network structure, and $\sigma_{CO_2} = 3.79$ Å, and $\varepsilon_{CO_2}/k_B = 225.3$ K, $\sigma_{CH_4} = 3.81$ Å, $\varepsilon_{CH_4}/k_B = 148.1$ K, and $\sigma_{N_2} = 3.69$ Å, and $\varepsilon_{N_2}/k_B = 96.3$ K [48]. For the cross-term LJ parameters, the Lorentz-Berthelot mixing rules were used to compute the size and energy parameters of the unlike molecules [68] by Eqs. (3) and (4):

$$\sigma_{12} = \frac{1}{2}(\sigma_1 + \sigma_2) \tag{3}$$

$$\varepsilon_{12} = \sqrt{\varepsilon_1 \varepsilon_2} \tag{4}$$

The molecule–molecule interactions were modeled with the cut and shifted LJ 6-12 potential by Eq. (5):

$$U(r) = \begin{cases} U_{LJ}(r) - U_{LJ}(r_c), & r \le r_c, \\ 0, & r > r_c \end{cases} \tag{5}$$

where $U_{LJ}(r)$ is the standard LJ potential by Eq. (6),

$$U_{LJ}(r) = 4\varepsilon\left\{\left(\frac{\sigma}{r}\right)^{12} - \left(\frac{\sigma}{r}\right)^{6}\right\} \tag{6}$$

Here, r is the distance between the interacting pair, and r_c is the cut-off distance $r_c = 4\sigma_{CH_4}$. Long-range corrections were not applied. Periodic boundary conditions were applied in y and z directions. All the quantities of interest are made dimensionless using CH_4 parameters, i.e., σ_{CH_4} and ε_{CH_4}; the reduced groups are listed in Table 1 [48].

To calculate the interactions between the fluid molecules and the walls, we used the LJ potential for the interactions between the molecules and the individual carbon atoms of the pore network structure. Previously it has been shown [45,47,48] that for gas mixtures under subcritical conditions, using a more realistic molecular representation of CO_2, i.e., a linear molecule with three LJ interaction sites on the three atoms plus point charges to account for the quadrupole moment, does not result in significantly different predictions, and therefore we do not employ that model for CO_2 in the current work. The cut-off distance between the molecules and the carbon atoms on the porous structure was $r_c = 3.5\sigma_{CH_4}$. The cut-off distance between the transport molecules and the carbon atoms in the porous structure was chosen to be slightly smaller than the cut-off distance of the molecule–molecule interaction in the fluid to speed up the calculations with minimal error. The interaction between the gas molecules with the entire carbon porous structure was taken to be the sum of the LJ potentials between the gas molecules and each individual carbon atom in the pore network structure. This is the most realistic interaction model with a porous structure in a computer simulation of confined fluids. However, this type of porous structure is computationally expensive to simulate, since fluid–fluid and fluid–carbon (surface) interactions in the pore network structure are calculated. To increase the computational speed, at the beginning of each simulation run, the simulation cell was divided into a large number of small subcells and a test particle was assigned to each subcell. The simulation cell was discretized into $n_x \times n_y \times n_z$ grid points along the three directions. We considered $n_x = 274$, $n_y = 181$, and $n_z = 182$, thus resulting in over 9000,000 small subcells. The test particle-porous structure interaction energies and their three derivatives, associated with all the subcells, were then calculated and recorded. To reduce the simulation time for the calculation of the interaction between a gas molecule and each of the carbon atoms in the porous structure we used a 3-D piecewise cubic Hermite interpolation [69,70], which interpolates a function and its first three derivatives to compute the potential energy and forces of a gas particle at any position using the previously recorded information at the $n_x \times n_y \times n_z$ grid points.

Flux and permeability of a fluid passing through the organic systems of the current study are important quantities of interest. Thus, for each component i we calculated its flux J_i in the direction of the applied chemical potential or pressure gradient. We calculated the flux J_i by measuring the net number of particles crossing a given yz plane of area A_{yz} using Eq. (7):

$$J_i = \frac{N_i^{LR} - N_i^{RL}}{N_{MD}\Delta t A_{yz}} \tag{7}$$

where N_i^{LR} and N_i^{RL} are the number of the molecules of type i moving from left to right and vice versa, respectively, Δt is the MD time step, and N_{MD} is the number of MD steps over which the average was taken (e.g., $N_{MD} = 50{,}000$). The system was considered to have reached steady state when the fluxes calculated at various yz planes were within 5% from the averaged values, after which the fluxes were calculated at the center of the transport region. The permeability K_i of component i was calculated using Eq. (8):

$$K_i = \frac{J_i}{\Delta P_i/L} = \frac{LJ_i}{\Delta P_i} \tag{8}$$

where $\Delta P_i = x_i \Delta P$ is the partial pressure drop for component i along the pore network, with x_i being the mole fraction of component i, and ΔP the total pressure drop imposed on the pore network. In what follows, we present and discuss the results of our simulation. The dimensions of the 3-D molecular pore network model are 102, 103, and 103 Å in x, y, and z directions, respectively. The pore network modeled large enough at the molecular scale that there will be no significant effect on the results by increasing the size of the simulation box [53]. Unless otherwise specified, all of the simulations were carried out with the upstream and downstream CVs being in equilibrium with a bulk fluid at a total pressure of 50 and 20 atm respectively. The temperature of the system was held constant at 25 °C.

It is worth mentioning that, if the porosity of a porous material is relatively large not too close to its percolation threshold [71] then often a single realization of the model produces the correct results. However, if the porosity is low, or if the system is close to a phase transition (which often happens at low temperatures), then, one must either generate several realizations of the model and average the results, or use a model with a large linear size. In the present work we used up to three realizations of the model pore

Table 1
The conversion between the dimensionless and the actual units. Subscript 1 refers to the value of the parameters for CH_4.

Variable	Reduced form
Length L	$L^* = L/\sigma_1$
Energy U	$U^* = U/\varepsilon_1$
Mass M	$M^* = M/M_1$
Density ρ	$\rho^* = \rho\sigma_1^3$
Temperature T	$T^* = k_B T/\varepsilon_1$
Pressure P	$P^* = P\sigma_1^3/\varepsilon_1$
Time t	$t^* = t(\varepsilon/M_1\sigma_1^2)$
Flux J	$J^* = J\sigma_1^3(M_1\varepsilon_1)^{1/2}$
Permeability K	$K^* = K(M_1\varepsilon_1)^{1/2}/\sigma_1$

networks, and averaged the results over them. In the current work the solid matrix of a graphite pore space is assumed to be a rigid structure, thus the swelling phenomena has not been considered.

5. Results and discussion

From a practical point of view, one of the most important properties to investigate and potentially predict is the permeability (Eq. (8)) of the gas components. Fig. 2 represents the dependence of CH_4, CO_2, and N_2 permeabilities on the porosity in the pore network with ~12.6 Å average pore size. The model shows that the permeability of all three components will increase with increasing porosity, as expected. In fact, as the Voronoi network models with higher porosity are generated having the same average pore size, the number and, therefore, the interconnectivity of the pores will increase, subsequently assisting molecular transport through the system. The permeability of all components is essentially *zero* until a critical porosity of about 20% is achieved, which is about the percolation threshold of the Voronoi structure [55]. Applying a larger upstream pressure and pressure gradient has minimal effect on the permeability when the porosity is low. The organic matrix of coal can often have low porosities [15,17–19]. Coal is highly heterogeneous and as such has highly variable physical (porosity pore size distribution, and pore connectivity) and chemical (adsorption, diffusion, permeability) properties that can change even across coals of similar rank [72]. This complexity poses challenges for modeling of gas flow and adsorption in these materials. Various studies have determined that coal permeabilities including the cleats range for from approximately 10 milliDarcy (mD) to 1 Darcy and for matrix permeability ranging from 0.04 to 0.7 mD [25,73–76]. These values were determined from coal sampled from the PRB, including Big George and Wyodak coals, based on interference tests from coal samples and history-matching production data from active coalbed methane (CBM) wells in the PRB. Studies on coal permeability have shown that coal structure and composition affect permeability [77,78] and also, it has been shown by Flores [75] and Stricker et al. [79] that coal lithotypes are highly heterogeneous within single coalbeds in the PRB. In another study by Huang and Shelton [80], the permeabilities of various coals reported in the range of 10 μD to 1 Darcy. However, the morphologies that include nano and microfractures may provide a more realistic representation of these systems. The fracture and pore networks are complex and are comprised of multi-scale structures. Fractures develop over a wide range of scales, and the coal matrix itself is not necessarily disconnected and isolated, as assumed in the double-porosity model [81]. The connectivity of the fracture networks in these systems to the pore-scale is still unknown as well as the size scale to which the fractures propagate. It has been shown that the inclusion of fractures can cause increases of up to two orders of magnitude in the prediction of permeability [82]. However, uncertainty exists, for example, a comprehensive literature search reveals only a few studies to date devoted to the detailed characterization of the cleat-fracture system including the cleat porosity, cleat spacing, and even cleat aperture [81,83,84]. The presence of fractures can also change coal stress-permeability behavior [82]. Fig. 3 shows the dependence of the CH_4, CO_2, and N_2 permeabilities on the average pore size in the pore network when the porosity is 25%. The results show that for this porosity, there is a maximum in permeability when the average pore size is approximately 12 Å. When the average pore sizes become larger, the permeabilities will also increase as the pore interconnectivity will increase and both convection and diffusion of fluid molecules increase.

In the pore network the permeabilities of CH_4, CO_2, and N_2 vary non-monotonically with increasing pressure drop (ΔP) along the pore network. This is demonstrated in Fig. 4, where we show the permeabilities of these components. In this figure, the porosity in the pore network is 35%, and the downstream pressure is fixed at 20 atm, while the upstream pressure varies. As the average pore size of the pore network decreases, the effect of molecular sieving is more pronounced. To demonstrate this, we present in Fig. 5 the permeabilities of the same components as in Fig. 4, and under precisely the same conditions, except that the average pore size in the pore network is 8.7 Å. Fig. 5 shows that the permeability of CO_2 is smaller than N_2 and CH_4 due to the molecular sieving and adsorption effects; however, the permeabilities of all components are lower than those shown in Fig. 4, since the pore sizes in the pore network are smaller, with their average size being approximately 8.7 Å, and it is more difficult for the molecules to be transported within the pore network.

Fig. 6 represents the time-averaged density profiles of N_2 and CO_2(top), and CH_4 and CO_2 (bottom) in an equimolar mixture of the two molecules as a function of $X^* = X/\sigma_{CH_4}$ along the pore network, defined as the region, $-13.4 < X^* < 13.4$. The average pore size and the porosity of the pore network is 12.5 Å and 25%

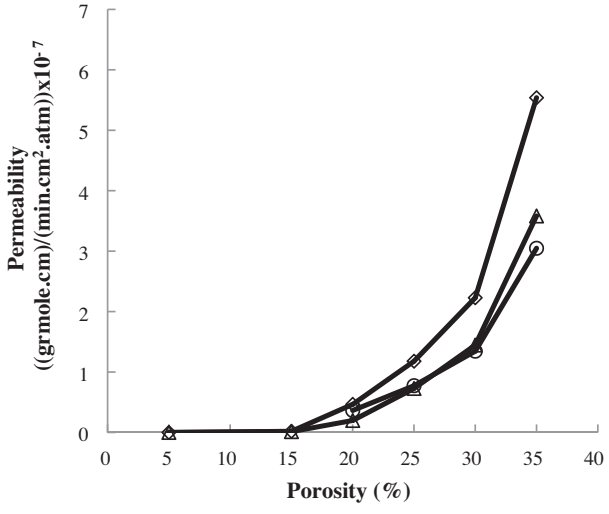

Fig. 2. The dependence of the permeability of CH_4 (diamonds), CO_2 (triangles), and N_2 (circles) on the porosity. The average pore size in the pore network is 12.6 Å.

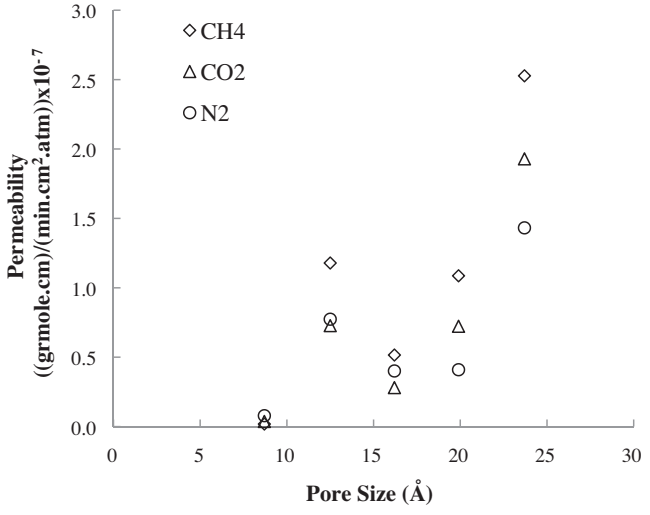

Fig. 3. The dependence of the permeability of CH_4 (diamonds), CO_2 (triangles), and N_2 (circles) on the average pore size in pore network. The porosity of the pore network is 25%.

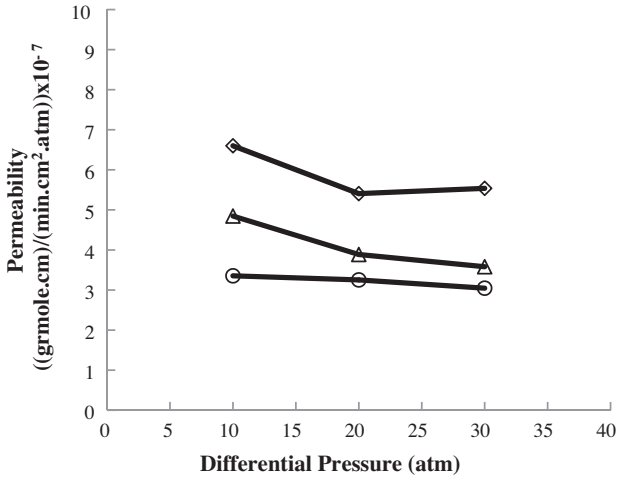

Fig. 4. The dependence of permeability of CH_4 (diamonds), CO_2 (triangles), and N_2 (circles) on the pressure drop ΔP applied to the pore network. The downstream pressures are fixed at 20 (atm). The average pore size and the porosity of the pore network is 12.6 Å, 35% respectively.

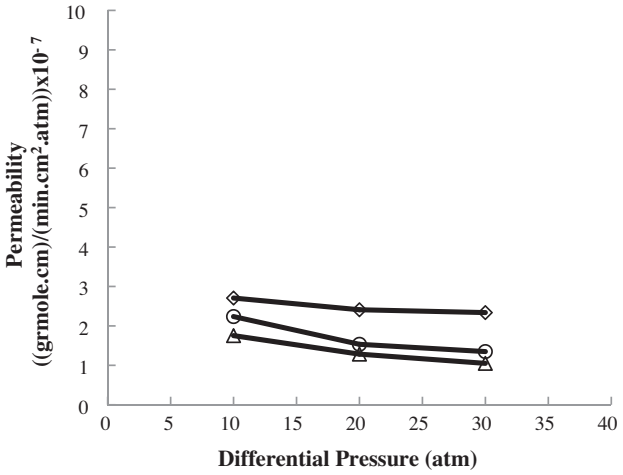

Fig. 5. The dependence of permeability of CH_4 (diamonds), CO_2 (triangles), and N_2 (circles) on the pressure drop ΔP applied to the pore network. The downstream pressures are fixed at 20 (atm). The average pore size and the porosity of the pore network is 8.7 Å, 35% respectively.

respectively. In this and the subsequent figures, the dashed lines indicate the boundaries of the pore network region. The density profiles are essentially flat in the two CVs, with numerical values that match those obtained by the GCMC method at the same conditions, indicating that the chemical potentials in the two CVs have been properly maintained during the NEMD simulations. The small downward curvature at $X^* = -40$, and $X^* = 40$ in the density profiles is due to the leakage of the particles out of the two CVs. These are the particles that, as discussed in Section 3, cross the outer boundaries of the CVs and leave the system. However, such deviations from a flat profile are insignificant. As can be seen from Fig. 6, the density of CO_2 rises sharply at the entrance to the carbon pore network, i.e., $X^* = -13.4$, and at the exit, $X^* = 13.4$. The adsorption affinity of the gases for the carbon surface causes this effect. Since the energy contribution for CO_2–carbon interactions is larger than that of the N_2–carbon and CH_4–carbon interactions, i.e., the carbon atom of the pore surface is more attractive to CO_2 than to N_2 and CH_4 molecules. The heights of the peaks in the density profiles of the gases in the mixtures exemplify this effect. On the other hand,

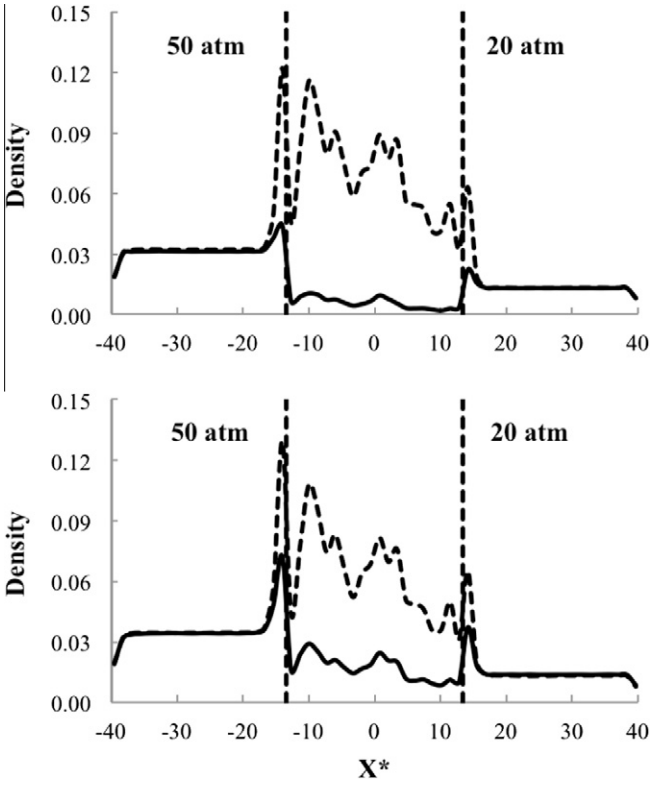

Fig. 6. Time-averaged density profiles of both components in an equimolar mixture of N_2 (solid curves) and CO_2 (dashed curves) (top), and in an equimolar mixture of CH_4 (solid curves) and CO_2 (dashed curves) (bottom), in the transport direction x. The average pore size and the porosity of the pore network is 12.5 Å, 25% respectively. Dashed lines indicate the boundaries of the pore network region.

since the energy parameter for the N_2–carbon interactions is weak in comparison to the other interactions, there is limited N_2 adsorption at the carbon pore network entrance and exit. This is the reason for smaller peaks present in the N_2 profile. In the transport region, i.e., $-13.4 < X^* < 13.4$, the densities for both components decrease along the pore network, which is expected. However, in both the equimolar mixture of N_2 and CO_2, and CH_4 and CO_2, the density of CO_2 is larger than that of N_2 and CH_4as CO_2has a high affinity for adsorption on the carbon surface. However, the density profiles in the transport region are not linear due to the existence of the overall bulk pressure gradient (or an overall nonzero streaming velocity). The diffusive and convective fluxes make up the total flux, which result in a nonlinear profile. At the same time, the porous carbon structure is heterogeneous with a range of the pore sizes and pore connectivities. Although the PSD is narrow, the porosity is relatively low and the pore space is still heterogeneous and, as a result, the density profiles are not necessarily smooth and monotonic, as they are in a single-pore system. In particular, they vary widely in the porous carbon-based materials. The temperature remains constant throughout the pore network and two CVs, hence, there is no contribution by a temperature gradient to the distribution of the molecules in the pore network. These features are clearly seen in Fig. 7, where we show snapshots of the same pore network and the distribution of the molecules for the same mixtures as in Fig. 6, obtained at steady state after 10^7 time steps. From the figure we can see that the densities of both components in the mixtures decrease from left to right, and the number of the CO_2 molecules in the pore network is larger than that of N_2 and CH_4 molecules in both mixtures.

Fig. 8 presents a snapshot of the same pore network and the molecular distribution for the same N_2 and CO_2 mixture as in

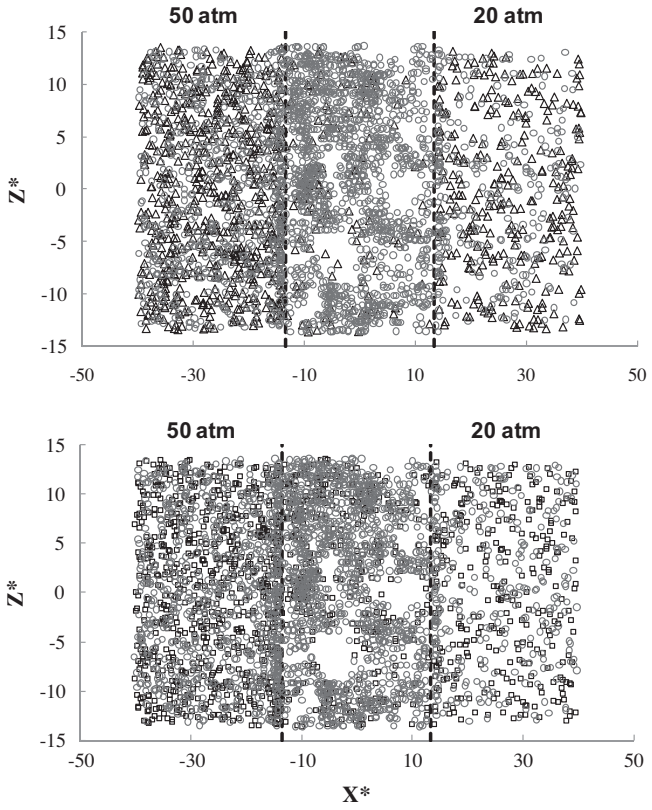

Fig. 7. Snapshots of the fluid molecules in the pore network containing an equimolar mixture of N_2 (triangles) and CO_2 (circles) (top), and in an equimolar mixture of CH_4 (squares) and CO_2 (circles) (bottom). The average pore size and the porosity of the pore network is 12.5 Å, 25%, respectively. Dashed lines indicate the boundaries of the pore network region.

Fig. 6, obtained at steady state after 10^7 time steps, except that the porosity in the pore network is increased to 35%. In both Figs. 7 and 8, the white spots in the pore network regions represent graphite where the fluid molecules cannot enter. A comparison of Figs. 7 and 8 indicates that having the same average pore size in the pore network as the porosity increases, the number of the pores will increase since more polyhedra need to be chosen to create the pores for obtaining increased porosity. As the number of pores increases, the likelihood that the pores become connected will also increase, and the density of both components in the pore network will subsequently increase. Fig. 9 compares the time-averaged density profiles of N_2 and CO_2 in a mixture with 25% CO_2. All qualitative

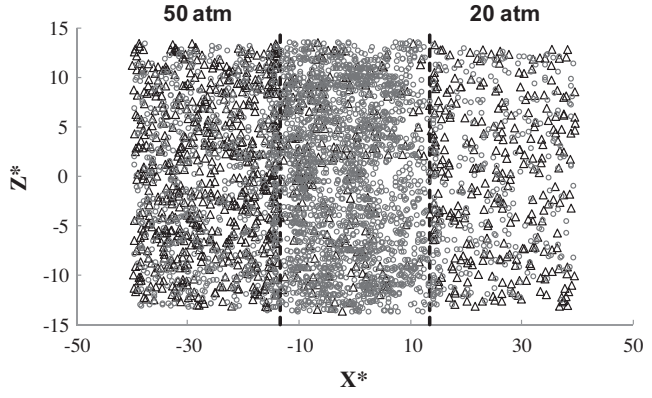

Fig. 8. Snapshots of both N_2 and CO_2 molecules in the pore network containing an equimolar mixture of N_2 (triangles) and CO_2 (circles). The average pore size and the porosity of the pore network is 12.6 Å, 35%, respectively. Dashed lines indicate the boundaries of the pore network region.

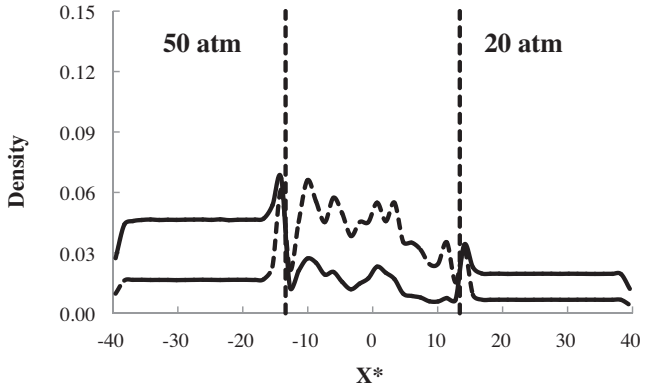

Fig. 9. Time-averaged density profiles of both components of N_2 (solid curves) and CO_2 (dashed curves) in the transport direction *x*. The mole fraction of CO_2 in the mixture is 0.25. The average pore size and the porosity of the pore network is 12.5 Å, 25%, respectively. Dashed lines indicate the boundaries of the pore network region.

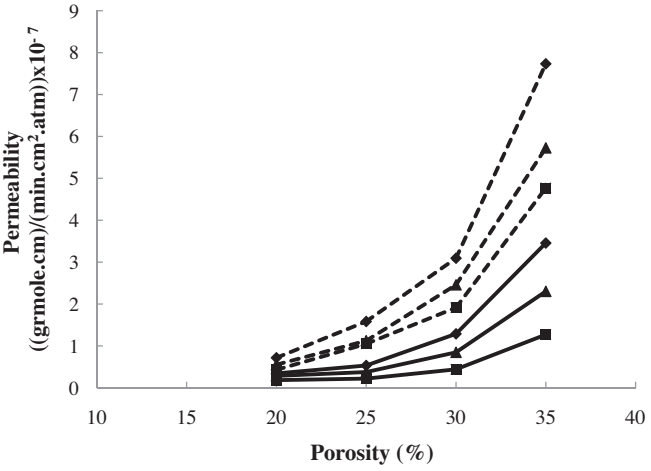

Fig. 10. The dependence of permeability of CH_4 (solid curves) and CO_2 (dashed curves) in the mixture on the porosity. The mole fraction of CH_4 in the mixtures are 0.75 (diamonds), 0.5 (triangles), and 0.25 (squares). The average pore size in the pore network is ~12.5 Å.

features of the profiles are similar to those shown in Fig. 6 except that, when the mole fraction of CO_2 is lower, the differences between the density profiles of two components in the pore network is not as large as those shown in Fig. 6. Clearly, despite the mixture being rich in N_2 and having higher N_2 density in the two CVs, there is still significantly more CO_2 in the pore network than N_2, which is again attributed to the higher adsorption of CO_2 on the carbon surface as described previously.

The dependence of permeabilities of two components in the mixture of CH_4 and CO_2 on the porosity is shown in Fig. 10. In this figure, the average pore size in the pore network is 12.6 Å, and the mole fraction of CO_2 in the mixture will change as shown in Fig. 10. Similar to Fig. 2, the results show that the permeability of both components will increase with increasing porosity, as the porosity of the generated Voronoi networks is higher, assisting in molecular transport through the pore network. The permeability of CO_2 is higher than CH_4 for the same porosity due to the higher and faster adsorption [85,86] and the shielding effect described earlier. It is also shown that CO_2 diffuses through the coal at a faster rate than methane, as expected [87]. As the mole fraction of CH_4 increases in the feed, the permeability of CH_4 will increase. The permeability of CH_4 is less affected by both the porosity and the feed composition,

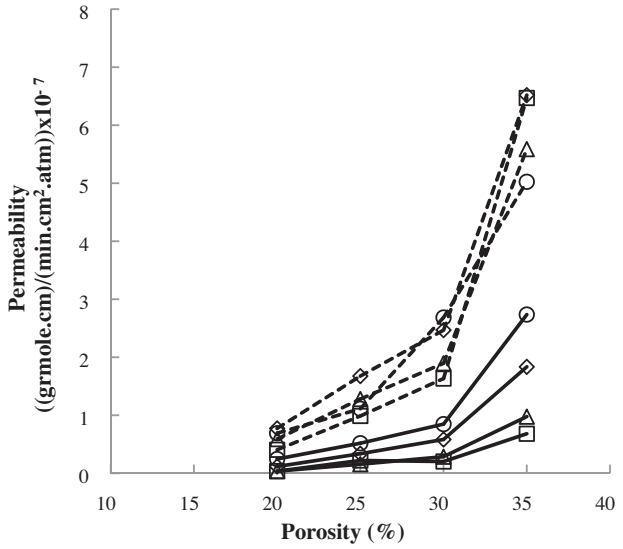

Fig. 11. The dependence of permeability of N_2 (solid curves) and CO_2 (dashed curves) in the mixture on the porosity. The mole fraction of N_2 in the mixtures are 0.88 (circles), 0.75 (diamonds), 0.5 (triangles), and 0.25 (squares). The average pore size in the pore network is ~12.5 Å.

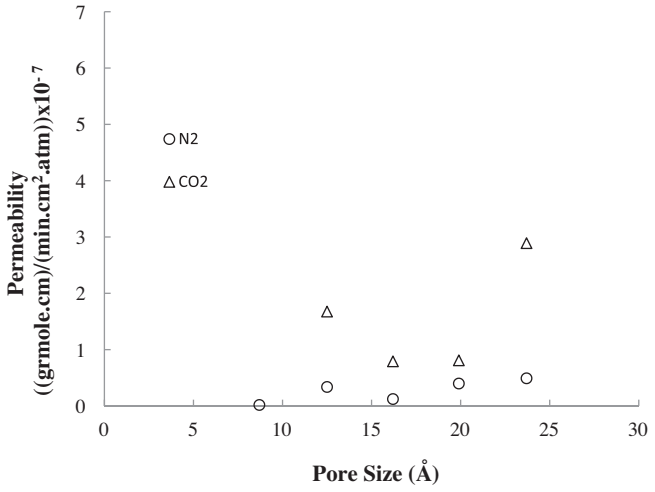

Fig. 12. The dependence of permeability of N_2 (circles) and CO_2 (triangles) in the mixture on the average pore size in the pore network. The mole fraction of CO_2 in the mixtures is 0.25 and the porosity is 25%.

while the permeability of CO_2 appears to depend rather strongly on the porosity and feed composition. Fig. 11 represents the dependence of permeabilities of two components in the mixture of N_2 and CO_2 on the porosity. The average pore size in the pore network is 12.6 Å, and the mole fraction of CO_2 in the mixture will change as shown in Fig. 11. All the qualitative features of the profiles are similar to those shown in Fig. 10.

Fig. 12 represents the dependence of both N_2 and CO_2 permeabilities in the mixture on the average pore size in the pore network. The mole fraction of CO_2 in the feed was 0.25, and the porosity 25%. The permeability of N_2 is affected only weakly by the pore size, while the permeability of CO_2 appears to depend rather strongly the pore size. Similar trends obtained as described in Fig. 3, in which the CO_2 permeability attains a maximum when the average pore size is approximately 12 Å. When the average pore size becomes larger, the permeabilities will also increase as the pore interconnectivity increases and both convection and diffusion of the CO_2 molecules increase.

6. Conclusions

Extensive molecular simulations were carried out to study the sensitivity of transport properties of carbon dioxide, methane and nitrogen as well as mixtures of nitrogen and carbon dioxide and methane and carbon dioxide on pore size, porosity and applied pressure gradient in carbon-based systems represented by 3-D pore networks. The results in this paper indicate that among these factors, the porosity of the structure strongly affects the permeability. In particular, the permeability is *zero* below a critical porosity of about 20% due to the low connectivity of the pore network. Also, more complex molecular models need to be investigated to model graphite structures containing defect sites and vacancies within the pore network, and the inclusion of chemical functional groups inside the cavities to generate more realistic 3-D coal structures. The influence of water, carbon monoxide and N- and S-containing functional groups will also be considered in future work. These results will have important implications for understanding the kinetics of CO_2 adsorption processes in addition of providing knowledge on the physics associated with CO_2 storage in carbon-based geologic formations.

Acknowledgements

We are grateful to the Department of Energy – National Energy Technology Laboratory for partial support of this work. Additionally, we wish to acknowledge discussions with Professors Mark Zoback and Anthony Kovscek that have helped us to advance this research. The computations were carried out on the Center for Computational Earth and Environmental Science (CEES) cluster at Stanford University. Also, we would like to thank Dennis Michael for administering the CEES cluster in addition to the MD code installation.

References

[1] T.X. Nguyen, S.K. Bhatia, Langmuir 24 (2008) 146.
[2] MacKinsey, Pathways to a low-carbon economy. Version 2 of the global greenhouse gas abatement cost curve, 2009.
[3] N. Stern, The Economics of Climate Change: The Stern Review, PART III: The Economics of Stabilisation, Cambridge University Press, 2007.
[4] J. PrzepiÓrski, M. Skrodzewicz, A.W. Morawski, Appl. Surf. Sci. 225 (2004) 235.
[5] A. Somy, M.R. Mehrnia, H. Delavari Amrei, A. Ghanizadeh, M. Safari, Int. J. Greenhouse Gas Control 3 (2009) 249.
[6] A. Busch, Y. Gensterblum, B.M. Krooss, R. Littke, Int. J. Coal Geol. 60 (2004) 151.
[7] J.E. Fitzgerald, Z. Pan, M. Sudibandriyo Jr., R.L. Robinson, K.A.M. Gasem, S. Reeves, Fuel 84 (2005) 2351.
[8] M. Mastalerz, H. Gluskoter, J. Rupp, Int. J. Coal Geol. 60 (2004) 43.
[9] S. Mazumder, P.V. Hemert, A. Busch, K-H.A.A. Wolf, P. Tejera-Cuesta, Int. J. Coal Geol. 67 (2006) 267.
[10] S. Ottiger, R. Pini, G. Storti, M. Mazzotti, R. Bencini, F. Quattrocchi, G. Sardu, G. Deriu, Environ. Prog. 25 (2006) 355.
[11] C.M. White, D.H. Smith, K.L. Jones, A.L. Goodman, S.A. Jikich, R.B. LaCount, S.B. DuBose, E. Ozdemir, B.I. Morsi, K.T. Schroeder, Energy Fuels 19 (2005) 659.
[12] H. Hu, X. Li, Z. Fang, N. Wei, Q. Li, Energy 35 (2010) 2939.
[13] P.D. Gamson, B.B. Beamish, D.P. Johnson, Fuel 72 (1993) 87.
[14] A.G. Jr. Sharkey, J.T. McCartney, Chemistry of coal utilization, second supplementary volume. Elliott, M.A., Ed., Wiley, New York, 1981, 159.
[15] F.Y. Wang, Z.H. Zhu, P. Massarotto, V. Rudolph, Chem. Eng. Sci. 62 (2007) 3268.
[16] International Union of Pure and Applied Chemistry (IUPAC), Manual of Symbols and Terminology for Physico Chemical Quantities and Units. Butterworth: London, U.K., 1972.
[17] S.J.M. Butala, J.C. Medina, T.Q. Taylor, C.H. Bartholomew, M.L. Lee, Energy Fuels 14 (2000) 235.
[18] H. Gan, S.P. Nandi, P.L. Jr Walker, Fuel 51(1972) 272.
[19] W.E. White, C.H. Bartholomew, W.C. Hecker, D.M. Smith, Adsorpt. Sci. Technol. 7 (1990) 180.
[20] G. Chen, S. Harpalani, Study of fracture network in coal, in: L.R. Myer, N.G.W. Cook, R.E. Goodman, C.-F. Tsang (Eds.), Fractured and jointed rock masses, Balkema, Rotterdam, 1995, p. 431.
[21] B.W. Gash, Log Anal. 33 (1992) 176.
[22] S.E. Laubach, R.A. Marrett, J.E. Olson, A.R. Scott, Int. J. Coal Geol. 35 (1998) 175.
[23] R. Puri, J.C. Evanoff, M.L. Brugler, SPE Gas Technology Symposium, 93, 22–24 January 1991, Houston, Texas.

[24] Advanced Resources International, Inc., Powder River Basin coalbed methane development and produced water management. Report DOE/NETL-2003/1184, 2002.
[25] M.J. Mavor, B. Russell, T.J. Pratt, Powder River Basin Ft. Union coal reservoir properties and production decline analysis. Paper SPE 84427, Presented at the SPE Annual Technical Conference and Exhibition, Denver, Colorado, October 5–8, 2003.
[26] M.R. Narkiewicz, J.P. Mathews, Energy Fuels 23 (2009) 5236.
[27] T.J. Tambach, J.P. Mathews, F.V. Bergen, Energy Fuels 23 (2009) 4845.
[28] J.C. Palmer, J.K. Brennan, M.M. Hurley, A. Balboa, K.E. Gubbins, Carbon 47 (2009) 2904.
[29] R.F. Cracknell, D. Nicholson, N. Quirke, Phys. Rev. Lett. 74 (1995) 2463.
[30] D.M. Ford, E.D. Glandt, J. Phys. Chem. 99 (1995) 11543.
[31] D.M. Ford, G.S. Heffelfinger, Mol. Phys. 94 (1998) 673.
[32] S. Furukawa, K. Hayashi, T. Nitta, J. Chem. Eng. Jpn. 30 (1997) 1107.
[33] G.S. Heffelfinger, F.V. Swol, J. Chem. Phys. 100 (1994) 7548.
[34] G.S. Heffelfinger, D.M. Ford, Mol. Phys. 94 (1998) 659.
[35] S. Kjelstrup, B. Hafskjold, Ind. Eng. Chem. Res. 35 (1996) 4203.
[36] M. Lupkowski, F.V. Swol, J. Chem. Phys. 95 (1991) 1995.
[37] J.M.D. MacElroy, J. Chem. Phys. 101 (1994) 5274.
[38] E.J. Maginn, A.T. Bell, D.N. Theodorou, J. Phys. Chem. 97 (1993) 4173.
[39] D. Nicholson, R.F. Cracknell, N. Quirke, Langmuir 12 (1996) 4050.
[40] P.I. Pohl, G.S. Heffelfinger, J. Membr. Sci. 155 (1999) 1.
[41] M. Sun, C. Ebner, Phys. Rev. A: At. Mol. Opt. Phys. 46 (1992) 4813.
[42] S. Sunderrajan, C.K. Hall, B.D. Freeman, J. Chem. Phys. 105 (1996) 1621.
[43] A.P. Thompson, D.M. Ford, G.S. Heffelfinger, J. Chem. Phys. 109 (1998) 6406.
[44] L. Xu, M.G. Sedigh, M. Sahimi, T.T. Tsotsis, Phys. Rev. Lett. 80 (1998) 3511.
[45] L. Xu, T.T. Tsotsis, M. Sahimi, J. Chem. Phys. 111 (1999) 3252.
[46] L. Xu, T.T. Tsotsis, M. Sahimi, Phys. Rev. E: Stat., Nonlinear, Soft Matter Phys. 62 (2000) 6942.
[47] L. Xu, M.G. Sedigh, T.T. Tsotsis, M. Sahimi, J. Chem. Phys. 112 (2000) 910.
[48] M. Firouzi, T.T. Tsotsis, M. Sahimi, J. Chem. Phys. 119 (2003) 6810.
[49] M. Firouzi, Kh. Molaai Nezhad, T.T. Tsotsis, M. Sahimi, J. Chem. Phys. 120 (2004) 8172.
[50] M. Firouzi, M. Sahimi, T.T. Tsotsis, Phys. Rev. E: Stat., Nonlinear, Soft Matter Phys. 73 (2006) 036312.
[51] M. Firouzi, T.T. Tsotsis, M. Sahimi, Chem. Eng. Sci. 62 (2007) 2777.
[52] N. Rajabbeigi, B. Elyassi, T.T. Tsotsis, M. Sahimi, J. Membr. Sci. 335 (2009) 5.
[53] N. Rajabbeigi, T.T. Tsotsis, M. Sahimi, J. Membr. Sci. 345 (2009) 323.
[54] G.R. Jerauld, J.C. Hatfield, L.E. Scriven, H.T. Davis, J. Phys. C: Solid State Phys. 17 (1984) 1519.
[55] G.R. Jerauld, L.E. Scriven, H.T. Davis, J. Phys. C: Solid State Phys. 17 (1984) 3429.
[56] M. Sahimi, T. Tsotsis, Ind. Eng. Chem. Res. 36 (1997) 3043.
[57] L. Xu, T.T. Tsotsis, M. Sahimi, J. Chem. Phys. 114 (2001) 7196.
[58] J. Ghassemzadeh, L. Xu, T.T. Tsotsis, M. Sahimi, J. Phys. Chem. B 104 (2000) 3892.
[59] H. Dominguez, M. Rivera, Mol. Phys. 100 (2002) 3829.
[60] M. Rivera, H. Dominguez, Mol. Phys. 101 (2003) 2953.
[61] K.K. Unger, J. Rouquerol, K.S.W. Sing, H. Kral (Eds.), Characterization of Porous Solids, Slsevier, Amsterdam, 1988.
[62] L.J. Gibson, M.F. Ashby, Cellular Solids, 2nd ed., Cambridge University Press, Cambridge, 1997.
[63] M. Sahimi, Flow and Transport Through Porous Media and Fractured Rock, VCH, Weinheim, 1995.
[64] P.T. Cromwell, Polyhedra, Cambridge University Press, Cambridge, 1997.
[65] M. Firouzi, "Molecular Simulation of the Structure, Transport, and Separation of Fluid Mixtures in Nanoporous Membranes under Subcritical and Supercritical Conditions" 2005.
[66] J.K. Johnson, J.A. Zollweg, K.E. Gubbins, Mol. Phys. 78 (1993) 591.
[67] D.M. Ruthven, Principles of adsorption & adsorption processes, John Wiley & Sons, 1984.
[68] M.P. Allen, D.J. Tildesley, Computer Simulation of Liquids, Oxford University Press, Oxford, 1987.
[69] D. Kahaner, C. Moler, S. Nash, Numerical Methods and Software, Prentice-Hall, Englewood Cliffs, New Jersey, 1989.
[70] M.H. Schultz, Spline Analysis, Prentice-Hall, Englewood Cliffs, New Jersey, 1973.
[71] M. Sahimi, Applications of Percolation Theory, Taylor & Francis, London, 1994.
[72] H.E. Ross, P. Hagin, M.D. Zoback, Int. J. Greenhouse Gas Control 3 (2009) 773.
[73] U.S. Geological Survey National Oil and Gas Resource Assessment Team, 1995 National assessment of United States oil and gas resources. U.S. Geological Survey Circular 1118, 1995.
[74] W. Ayers, AAPG Bull. 86 (2002) 1853.
[75] R.M. Flores, Coalbed Methane in the Powder River Basin, Wyoming and Montana: an Assessment of the Tertiary-Upper Cretaceous Coalbed Methane Total Petroleum System. U.S. Geological Survey Digital Data Series DDS-69-C, Chapter 2, 2004.
[76] G. Twombly, S.H. Stepanek, T.A. Moore, Coalbed methane potential in the Waikato Coalfield of New Zealand: a comparison with developed basins in the United States. 2004 New Zealand Petroleum Conference Proceedings, March 7–10, Ministry of Economic Development, Auckland, New Zealand, unpaginated, 2004.
[77] R.M. Bustin, AAPG Bull. 81 (1997) 1894.
[78] C.R. Clarkson, R.M. Bustin, Int. J. Coal Geol. 33 (1997) 135.
[79] G.D. Stricker, R.M. Flores, D.E. McGarry, D.P. Stillwell, D.J. Hoppe, C.R. Stillwell, A.M. Ochs, M.S. Ellis, K.S. Osvald, S.L. Taylor, M.C. Thorvaldson, M.H. Trippi, S.D. Grose, F.J. Crockett, A.J. Shariff, Gas desorption and adsorption isotherm studies of coals in the Powder River Basin, Wyoming and adjacent basins in Wyoming and North Dakota. U.S. Geological Survey Open-File Report 2006-1174, 2006.
[80] W.H. Huang, T.C. Shelton, Min. Eng. 14 (1962) 52.
[81] T.T. Tsotsis, H. Patel, B. Fayyaz Najafi, D. Racherla, M.A. Knackstedt, M. Sahimi, Ind. Eng. Chem. Res. 43 (2004) 2887.
[82] S. Durucan, J.S. Edwards, Min. Sci. Technol. 3 (1986) 205.
[83] S. Harpalani, X. Zhao, Energy Sources 13 (1991) 229.
[84] S. Harpalani, S. Ouyang, G. Chen, Transaction, Soc. Min. Metall. Explor., INC 300 (1996), 108.
[85] D. Li, Q. Liu, P. Weniger, Y. Gensterblum, A. Busch, B.M. Krooss, Fuel 89 (2010) 569.
[86] M.S. Gruszkiewicz, M.T. Naney, J.G. Blencoe, D.R. Cole, J.C. Pashin, R.E. Carroll, Int. J. Coal Geol. 77 (2009) 23.
[87] J.D.N. Pone, P.M. Halleck, J.P. Mathews, Energy Fuels 23 (2009) 4688.